Giant Second-Harmonic Generation Response and Large Bandgap in the Partially-Fluorinated Mid-Infrared Oxide $RbTeMo_2O_8F$

Yilei Hu,[†,δ] Chao Wu,[†,δ] Xingxing Jiang,[‡,δ] Hongyuan Sha,[†] Zhipeng Huang,[†] Zheshuai Lin,[‡] Mark G. Humphrey,[§] and Chi Zhang[†,*]

[†] China-Australia Joint Research Center for Functional Molecular Materials, School of Chemical Science and Engineering, Tongji University, Shanghai 200092, China

[‡] Key Lab of Functional Crystals and Laser Technology, Technical Institute of Physics and Chemistry, Chinese Academy of Sciences, Beijing 100190, China

[§] Research School of Chemistry, Australian National University, Canberra, ACT 2601, Australia

* Email: chizhang@tongji.edu.cn

[δ] Y.L.H., C.W. and X.X.J. contributed equally to this paper

Supporting Information Placeholder

ABSTRACT: Strong second-harmonic generation (SHG) and a wide bandgap are two crucial but often conflicting parameters that must be optimized for practical nonlinear optical (NLO) materials. We report herein the first example of a d^0-TM tellurite where half of the d^0-transition-metal octahedra are partially fluorinated, namely $RbTeMo_2O_8F$, which exhibits giant SHG responses (27 times that of KH_2PO_4 (KDP) and 2.2 times of $KTiOPO_4$ (KTP) with 1064 and 2100 nm laser radiation, respectively), the largest SHG values among all reported metal tellurites. $RbTeMo_2O_8F$ also possesses a large bandgap (3.63 eV), a wide optical transparency window (0.34–5.40 μm), and a significant birefringence (Δn: 0.263 at 546 nm). Theoretical calculations and crystal structure analysis demonstrate that the outstanding SHG responses can be definitively attributed to the uniform alignment of the polarized $[MoO_6]$/$[MoO_5F]$ octahedra and the seesaw-like $[TeO_4]$, and the consequent favorable summative polarization of the three distinct SHG-active polyhedra, both induced by partial fluorine substitution on the $[MoO_6]$ octahedra.

Nonlinear optical (NLO) crystals are a key component for switching laser sources to new spectral regions through frequency-conversion technology.[1,2] Mid-infrared (mid-IR, 3−5 μm) lasers are essential for applications in many fields, such as medical treatment, military communication, and laser lithography.[3-5] Chalcogenides $AgGaS_2$ (AGS) and $AgGaSe_2$, and pnictide $ZnGeP_2$ (ZGP) are well-known mid-IR NLO crystals[6] due to their superior IR transparency and second-harmonic generation (SHG) effect. Unfortunately, inherent drawbacks such as relatively narrow band gaps, low laser damage thresholds (LDTs), two-photon absorption, and/or non-phase matchability greatly limit their practical NLO applications.[7] As a result, the development of new mid-IR NLO materials with both a strong SHG effect and a wide band gap is of significant academic and commercial interest.[7-9]

Metal oxides based on lone-pair oxyanions, including iodates,[10-12] selenites,[13,14] and tellurites,[15,16] have been a focus of NLO materials research, because they usually exhibit a large bandgap, a wide optical transparency range, and ease of crystal growth. However, the SHG efficiencies of most lone-pair oxyanion-based oxides lacking additional NLO-active structural units are not demonstrably superior to those of commercialized mid-IR chalcogenides. d^0-Transition metal (TM)-centered polyhedra susceptible to second-order Jahn−Teller (SOJT) distortions[17,18] have been introduced into lone-pair oxyanion-based oxide systems to enhance their SHG efficiency, examples including $Li_2Ti(IO_3)_6$ (SHG efficiency 500 × α-SiO_2, band gap 3.00 eV),[19] $K(VO)_2O_2(IO_3)_3$ (3.6 × $KTiOPO_4$ (KTP), 2.30 eV),[20] $Cs_2(MoO_3)_3(SeO_3)$ (350 × α-SiO_2, 3.10 eV),[21] $Cs_2TeMo_3O_{12}$ (400 × α-SiO_2, 2.88 eV),[22] $BaTeMo_2O_9$ (600 × α-SiO_2, 3.26 eV)[23] and $BaTeW_2O_9$ (500 × α-SiO_2, 3.42 eV).[23] Despite these successes, the incorporation of multiple TM-centered units to construct efficient NLO oxides simultaneously possessing strong SHG effects (> 10 × KH_2PO_4 (KDP)[24,25] and large band gaps (> 3.5 eV) is thus far underexploited because of the unfavorable arrangements of multiple SHG-active groups and/or undesirable electronic transitions of the d^0-TM cations.[26]

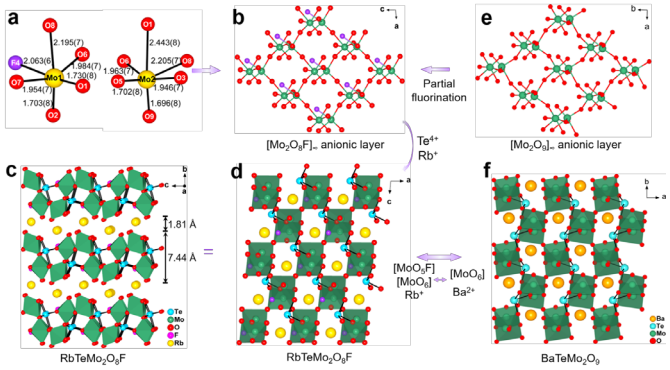

Figure 1. (a) The $[MO_5F]$ and $[MO_6]$ units. (b) View of the $[Mo_2O_8F]_\infty$ anionic layer of $RbTeMo_2O_8F$ in the *ac* plane. (c) View of $RbTeMo_2O_8F$ along the *a*-axis. (e) View of the $[Mo_2O_9]_\infty$ anionic layer of $BaTeMo_2O_9$ in the *ab* plane. Structural comparison of $RbTeMo_2O_8F$ (d) and $BaTeMo_2O_9$ (f).

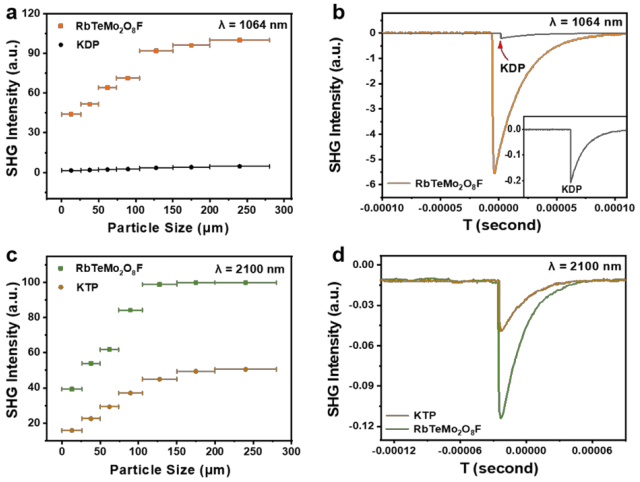

Figure 2. Phase-matching curves of $RbTeMo_2O_8F$ with 1064 nm (a) and 2100 nm (c) laser radiation. Oscilloscope traces of the SHG signals (105−150 μm) at λ = 1064 nm (b) and 2100 nm (d). KDP and KTP samples serve as the references.

Correlations between the molecular structures and NLO properties of SHG oxide crystals have revealed the subtle influence of the composition, arrangement, and packing configuration of the SHG-active units on linear optical and NLO performance. In particular, the introduction of polarizing elements[27] may favor both the construction of highly polarizable structural units and the enhancement of the optical bandgap. In the present study, we propose a partial fluorine substitution strategy to increase structural distortion of lone-pair oxyanion-based TM oxides. Replacing one oxygen site in half of the d^0-TM centered octahedra with more highly electronegative fluorine may induce significant differences in the band structures and, by this means, potentially improve the bandgaps and SHG responses.[19,28] In addition, the fluorine may act as a structure directing agent,[29] aligning the asymmetric metal-oxyfluoride units preferentially in one direction,andtherebyforming a macroscopic polar compound, for which optimized SHG efficiency may be achieved by stacking the discrete NLO-active structural units in an additive mode. Following this strategy, the first example of a d^0-TM tellurite where half of the d^0-transition-metal octahedra are partially fluorinated, namely $RbTeMo_2O_8F$, has been constructed, which exhibits giant SHG responses in both the visible (27 × KDP @ 1064 nm) and IR (2.2 × KTP @ 2100 nm) spectral ranges, as well as a large band gap (3.63 eV), a sufficient birefringence (0.263 @ 546 nm) for phase-matching, and a wide optical transparency range covering the important mid-IR (3−5 μm) window. Herein, we report its synthesis, crystal structure, linear and nonlinear optical properties, and computational studies to rationalize its excellent optical performance.

Single crystals of $RbTeMo_2O_8F$ were synthesized via the hydrothermal method from a mixture of Rb_2CO_3, MoO_3, TeO_2, hydrofluoric acid, and deionized water (see Supporting Information for details). The purity of the crystalline sample was confirmed by powder X-ray diffraction (PXRD) (Figure S1). The Rb, Mo, Te, and F content of the crystal was confirmed by microprobe energy-dispersive spectroscopy (EDS) (Figure S2). Thermogravimetric analysis (TGA) indicates that $RbTeMo_2O_8F$ is thermally stable up to 758 °C (Figure S3).

$RbTeMo_2O_8F$ crystallizes in the noncentrosymmetric space group *Pn* (no. 7) (Tables S1−S3). Unlike the previously reported fluorine-free molybdenum tellurites, $RbMo_2TeO_8F$ features a unique two-dimensional (2D) layered structure $[Mo_2O_4F(TeO_4)]$ that is composed of $[MoO_6]$ and the distinctive $[MoO_5F]$ octahedra and $[TeO_4]$ units, and with Rb^+ serving as the counter cations for charge balance (Figure 1c). It is noteworthy that the Mo^{6+} cations adopt two types of six-coordinate environments ($[Mo(1)O_5F]$ and $[Mo(2)O_6]$), with a wide range of Mo-O/F bond distances [1.696(5)−2.443(6) Å] (Figure 1a). The Te^{4+} cation exhibits a seesaw-like geometry with three normal Te-O bonds varying from 1.891(5) to 1.948(5) Å and one elongated Te-O bond (2.328(5) Å). Both Mo^{6+} and Te^{4+} cations are in asymmetric coordination environments attributable to SOJT effects. Each Rb^+ cation is 12-coordinated with one F atom and eleven O atoms (Figure S4). The Rb-O bonds range from 2.884(6) to 3.596(6) Å and the Rb-F bond is 2.778(4) Å. Bond valence sum (BVS) calculations reveal BVS values of 6.05−6.13 and 3.851 for Mo and Te, respectively, consistent with the coordination environments and anticipated formal oxidation states of the Mo and Te atoms.

From the viewpoint of structural evolution, $RbTeMo_2O_8F$ possesses a similar layered structure to that of $BaTeMo_2O_9$,[23] but one in which half of the $[MoO_6]$ units in the $[Mo_2O_9]_\infty$ layers of $BaTeMo_2O_9$ are replaced by partially fluorinated $[MoO_5F]$ octahedra (Figures 1b and 1e). The main difference between the two layered structures can be attributed to this partial introduction of fluorine atoms at the terminal sites of the $[MoO_6]$ octahedra. As a result, the structure of quinary $RbTeMo_2O_8F$ exhibits the following crucial differences to that of quaternary $BaTeMo_2O_9$: (i) The partial substitution of oxygen atoms with the strongly electronegative fluorine increases the bandgap remarkably from 3.12 to 3.63 eV (Table 1), which can be attributed to the increased ionicity of the Mo-F bonds.[19] (ii) The coordination environments of the Mo(1) atoms are significantly influenced by fluorine substitution. Specifically, both the $[MoO_5F]$ and the $[MoO_6]$ octahedra in $RbTeMo_2O_8F$ display an out-of-center distortion towards an edge (along the C_2 direction), while the Mo^{6+} cations in $BaTeMo_2O_9$ distort along the local C_3 direction towards a face of the $[MoO_6]$ octahedra. The out-of-center distortions[30] of the Mo-centered octahedra in $RbTeMo_2O_8F$ (Δd ($[MoO_5F]$) = 0.886, Δd ($[MoO_6]$) = 1.361) differ from those in $BaTeMo_2O_9$ (Δd ($[MoO_6]$) = 1.24, 1.229), with all Mo^{6+} cations displaying a strong distortion (Δd > 0.8). (iii) The $[Mo_2O_8F]_\infty$ layers lie in the *ac* plane in which the Te^{4+} cations of the $[TeO_4]$ units are also located. Due to the see-saw-like geometry, all the Te^{4+} lone-pair electrons are therefore constrained to point uniformly in the *a* direction (Figure 1d), a differing arrangement to that of $BaTeMo_2O_9$ (Figure 1f). This ordered arrangement should be immensely beneficial for enhancing the SHG response. (iv) The edge-sharing connection between the $[TeO_4]$ and $[MoO_6]$/$[MoO_5F]$ polyhedra favors the formation of a highly condensed layered-structure. All of these structural characteristics of the polar $RbTeMo_2O_8F$ contribute to the resultant favorable arrangement of all three NLO-active units, and thereby promote a large net macroscopic polarization and SHG response. Dipole moment calculations[32] of $RbTeMo_2O_8F$ and $BaTeMo_2O_9$ were undertaken to evaluate the polarization of the constituent groups. As shown in Table S4, the calculated dipole moment of $[MoO_6]$ is larger than that of $[MoO_5F]$, which is

in agreement with the out-of-center distortion calculation above. The magnitude of the dipole moment of a single [TeO_4] polyhedron (11.11 D) in $RbTeMo_2O_8F$ is close to that of a single [TeO_4] polyhedron (11.09 D) in $BaTeMo_2O_9$. However, $RbTeMo_2O_8F$ exhibits a net dipole moment (13.32 D) two-fold greater than that of $BaTeMo_2O_9$ (5.50 D). This is consistent with the observation above that the Te^{4+} lone-pair electrons are aligned in $RbTeMo_2O_8F$, while the dipole moments of the [TeO_4] polyhedra are nearly antiparallel in $BaTeMo_2O_9$. The distinctly different arrangements of these key SHG-active units contribute to the considerably larger SHG response of $RbTeMo_2O_8F$ than that of $BaTeMo_2O_9$.

The IR spectrum (Figure S5) and UV-Vis-NIR diffuse reflectance spectrum (Figure S6) of $RbTeMo_2O_8F$ showed a wide transparent region (ca. 0.34−5.40 μm), covering the visible and important mid-IR atmospheric transparency windows

Table 1. Comparison of the SHG Responses and Bandgaps of Tellurite-Based d^0-TM NLO Materials.

Formula	SHG-Active Units	SHG Efficiency	Bandgap(eV)
$Ag_2Te_3Mo_3O_{16}$[33]	$MoO_6/TeO_3/TeO_4$	8 × KDP[a]	2.85
$ZnTeMoO_6$[36]	$ZnO_6/MoO_4/TeO_4$	10.5 × KDP[a]	3.54
$CdTeMoO_6$[37]	$CdO_4/MoO_4/TeO_4$	2.0 × KTP[a]	3.59
$MnTeMoO_6$[32]	MoO_4/TeO_4	0.7 × KTP[b]	3.02
$TlTeVO_5$[31]	$TlO_8/VO_6/TeO_4$	40 × α-SiO_2[a]	2.16
$MgTeMoO_6$[34]	$MgO_6/MoO_4/TeO_4$	1.5 × KTP[a]	3.12
α-$BaTeMo_2O_9$[33]	$MoO_6/TeO_3/TeO_4$	0.2 × KDP[a]	3.12
$BaTeW_2O_9$[25]	WO_6/TeO_4	500 × α-SiO_2[a]	3.42
β-$BaTeMo_2O_9$[25]	MoO_6/TeO_4	600 × α-SiO_2[a]	3.26
$Na_2Te_3Mo_3O_{16}$[37]	$MoO_6/TeO_3/TeO_4$	500 × α-SiO_2[a]	2.95
$Na_2TeW_2O_9$[35]	WO_6/TeO_3	500 × α-SiO_2[a]	3.45
$Cs_2TeMo_3O_{12}$[24]	MoO_6/TeO_3	400 × α-SiO_2[a]	2.88
$Cs_2TeW_3O_{12}$[31]	WO_6/TeO_3	1.5 × KTP[a]	2.89
$RbTeMo_2O_8F$	$MoO_5F/MoO_6/TeO_4$	27 × KDP[a], 2.2 × KTP[b]	3.63

The SHG efficiency was measured at 1064 nm [a] and 2100 nm [b].

(3−5 μm). UV-Vis-NIR measurements revealed an absorption cutoff wavelength of 342 nm, corresponding to a wide bandgap of 3.63 eV. This value is not only significantly larger than that of the commercial IR NLO crystals $AgGaS_2$ (2.62 eV),[6] $AgGaSe_2$ (1.83 eV),[6] and $ZnGeP_2$ (1.99 eV),[6] but also larger than that of many excellent tellurites with [TeO_4] groups (Table 1).

According to the SHG measurement results (Figure 2), $RbTeMo_2O_8F$ exhibits a phase-matchable tendency towards both 1064 and 2100 nm radiation, and displays giant SHG responses of 27 × KDP (@ 1064 nm) and 2.2 × KTP (@ 2100 nm) in the 105−150 μm particle size range. These values are significantly larger than that of $BaTeMo_2O_9$ (600 × α-SiO_2)[24] and are the largest values of all reported tellurites (Table 1). The birefringence of $RbTeMo_2O_8F$ was measured on a selected single crystal using a ZEISS Axio A1 polarizing microscope. The crystal achieved complete extinction when the retardation value reached ca. 11.64 μm with a measured thickness of 44.2 μm (Figure S7); the birefringence was calculated to be 0.263 at 546 nm, sufficient to realize phase matchability.

The linear optical and NLO properties were further investigated by theoretical means. The electronic structure is depicted in Figure 3a, with a direct bandgap of 2.91 eV that is underestimated in comparison with the experimental result owing to the discontinuous exchange-correlation function. The calculated total and partial densities of states (Figure 3b) reveal that the electronic states of Mo 4*d* coincide with those of O 2*p* and F 2*p*, consistent with strong covalent interactions in the Mo-O/F bonds. The bottom of the conduction band (CB) is mainly occupied by Mo 4*d* and O 2*p* states while the top of the valence band (VB) has contributions mainly from O 2*p* states. The theoretical studies suggest that the optical properties of $RbTeMo_2O_8F$ are mainly determined by the [MoO_6], [MoO_5F], and [TeO_4] groups because the relevant virtual (electron and hole) excitations are between the states near the Fermi level which are dominated by these groups.

Under the restriction of Kleinman symmetry, $RbTeMo_2O_8F$ has six independent SHG tensors (d_{11}, d_{12}, d_{13}, d_{15}, d_{24}, and d_{33}), which are listed in Table S4. The largest SHG coefficient (d_{15}: 9.40 pm/V) was calculated to be 24 times that of KDP, which is consistent with the experimental powder SHG response. To shed further light on the significance of the $RbTeMo_2O_8F$ structure for its exceptional SHG properties, a real-space atom-cutting analysis was performed. The largest SHG component d_{15} is mostly attributed to the [MoO_6] (25.3%), [MoO_5F] (42.2%) and [TeO_4] (29.7%) groups while the alkali metal cation Rb^+ contributes little. The origin of the SHG effect was further investigated by performing an SHG-weighted electron density analysis (Figures 3c and 3d). It is clear that the SHG-weighted electron clouds are mainly

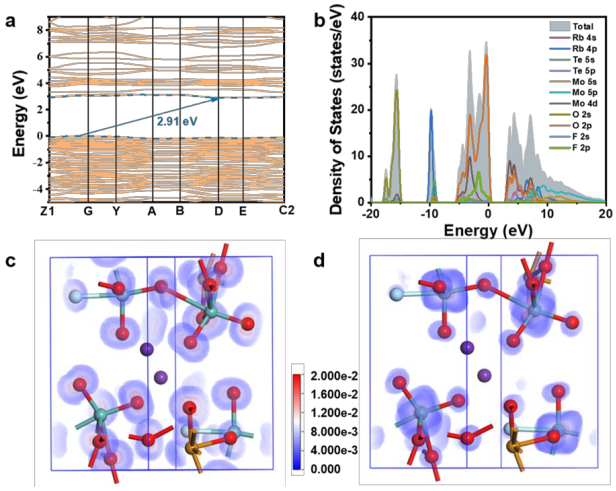

Figure 3. (a) Calculated band structure of $RbTeMo_2O_8F$. (b) Density of states (DOS) of $RbTeMo_2O_8F$. SHG-weighted electron clouds of the occupied (c) and unoccupied (d) states in the VE process. Color codes: Mo blue, Te yellow, O red, F light blue.

located on the [MoO_6] and [MoO_5F] octahedra and the [TeO_4] groups, consistent with the real-space atom-cutting results. The nonbonding O 2*p* and F 2*p* orbitals and the lone pairs on the Te^{4+} cations play an important role in the occupied states, while the SHG-weighted clouds for the unoccupied states are predominantly localized on the Mo 4*d* orbitals.

In summary, we have synthesized the first d^0-TM tellurite where half of the d^0-transition-metal octahedra are partially fluorinated. The quinary oxide $RbTeMo_2O_8F$ possesses three types of SHG-active units, [MoO_6], [MoO_5F] and [TeO_4], and exhibits the largest SHG responses for tellurites at both 1064 nm (27 × KDP) and 2100 nm (2.2 × KTP), an enlarged bandgap (3.63 eV), a wide infrared transparency window (0.34–5.40 μm), and a significant birefringence (Δn) of 0.263 at 546 nm that is suitable for phase-matching, which collectively indicate that $RbTeMo_2O_8F$ is an excellent candidate mid-IR NLO materials. Theoretical calculations confirm that the outstanding linear optical and NLO properties mostly stem from the favorable ordered alignment of the highly distorted [MoO_6], [MoO_5F] and [TeO_4] polyhedra. The study demonstrates a rare coexistence of giant SHG responses and large bandgap that has been achieved by the partial introduction of partially fluorinated d^0-TM octahedra into the tellurite system; accordingly, this provides an outstanding paradigm for the future development of high-performance mid-IR NLO crystalline materials.

ASSOCIATED CONTENT

This Supporting Information is available free of charge via the Internet at http://pubs.acs.org.

Experimental details, crystallographic data, IR and UV-vis-NIR spectra, EDS results, powder XRD patterns, TG analyses, theoretical calculations, and additional structures (PDF)
X-ray crystallographic file for CCDC number 2083010 (CIF)

ACKNOWLEDGMENT

This research was financially supported by National Natural Science Foundation of China (no. 51432006), Ministry of Education of China for Changjiang Innovation Research Team (no. IRT14R23), Ministry of Education and State Administration of Foreign Experts Affairs for 111 Project (no. B13025). M.G.H. thanks the Australian Research Council (DP170100411).

REFERENCES

(1) Cyranoski, D. Materials Science: China's Crystal Cache. *Nature* **2009**, *457*, 953-955.
(2) Mutailipu, M.; Poeppelmeier, K. R.; Pan, S. L. Borates: A Rich Source for Optical Materials. *Chem. Rev.* **2021**, *121*, 1130-1202.
(3) Chung, I.; Kanatzidis, M. G. Metal Chalcogenides: A Rich Source of Nonlinear Optical Materials. *Chem. Mater.* **2014**, *26*, 849-869.
(4) Chen, J. D.; Lin, C. S.; Zhao, D.; Luo, M.; Peng, G.; Li, B. X.; Yang, S. D.; Sun, Y. S.; Ye, N. Anionic Aliovalent Substitution from Structure Models of ZnS: Novel Defect Diamond-like Halopnictide Infrared Nonlinear Optical Materials with Wide Band Gaps and Large SHG Effects. *Angew. Chem. Int. Ed.* **2020**, *59*, 23549-23553.
(5) Zhang, H.; Zhang, M.; Pan, S. L.; Dong, X. Y.; Yang, Z. H.; Hou, X. L.; Wang, Z.; Chang, K. B.; Poeppelmeier, K. R. $Pb_{17}O_8Cl_{18}$: A Promising IR Nonlinear Optical Material with Large Laser Damage Threshold Synthesized in an Open System. *J. Am. Chem. Soc.* **2015**, *137*, 8360-8363.
(6) Nikogosyan, D. N. Nonlinear Optical Crystals: A Complete Survey, 1st ed.; Springer: New York, **2005**; pp 75-96.
(7) Wu, K.; Zhang, B. B.; Yang, Z. H.; Pan, S. L. New Compressed Chalcopyrite-like $Li_2BaM^{IV}Q_4$: Promising Infrared Nonlinear Optical Materials. *J. Am. Chem. Soc.* **2017**, *139*, 14885-14888.
(8) Guo, S. P.; Cheng, X. Y.; Sun, Z. D.; Chi, Y.; Liu, B. W.; Jiang, X. M.; Li, S. F.; Xue, H. G.; Deng, S. Q.; Duppel, V.; Kohler J.; Guo, G. C. Large second harmonic generation (SHG) effect and high laser-induced damage threshold (LIDT) observed coexisting in gallium selenide. *Angew. Chem. Int. Ed.* **2019**, *58*, 8087-8091.
(9) Li, R. A.; Zhou, Z. Y.; Lian, Y. K.; Jia, F.; Jiang, X. X.; Tang, M. C.; Wu, L. M.; Sun, J. L.; Chen, L. A_2SnS_5: A Structural Incommensurate Modulation Exhibiting Strong Second-Harmonic Generation and a High Laser-Induced Damage Threshold (A = Ba, Sr). *Angew. Chem. Int. Ed.* **2020**, *59*, 11861-11865.
(10) Hu, C. L.; Mao, J. G. Recent Advances on Second-Order NLO Materials Based on Metal Iodates. *Coord. Chem. Rev.* **2015**, *288*, 1-17.
(11) Nguyen, S. F.; Yeon, J.; Kim, S. H.; Halasyamani, P. S. $BiO(IO_3)$: A New Polar Iodate that Exhibits an Aurivillius-Type $(Bi_2O_2)^{2+}$ Layer and a Large SHG Response. *J. Am. Chem. Soc.* **2011**, *133*, 12422-12425.
(12) Wu, C.; Jiang, X. X.; Wang, Z. J.; Lin, L.; Lin, Z. S.; Huang, Z. P.; Long, X. F.; Humphrey, M. G.; Zhang, C. Giant Optical Anisotropy in the UV-Transparent 2D Nonlinear Optical Material $Sc(IO_3)_2(NO_3)$. *Angew. Chem. Int. Ed.* **2021,** *60*, 3464-3468.
(13) Liang, M. L.; Hu, C. L.; Kong, F.; Mao, J. G. $BiFSeO_3$: An Excellent SHG Material Designed by Aliovalent Substitution. *J. Am. Chem. Soc.* **2016**, *138*, 9433-9436.
(14) Chung, J. Y.; Jo, H.; Yeon, S.; Byun, H. R.; You, T. S.; Jang, J. I.; Ok, K. M. $Bi_3(SeO_3)_3(Se_2O_5)F$: A Polar Bismuth Selenite Fluoride with Polyhedra of Highly Distortive Lone Pair Cations and Strong Second-Harmonic Generation Response. *Chem. Mater.* **2020**, *32*, 7318-7326.
(15) Zhou, J. J.; Wu, H. P.; Yu, H. W.; Jiang, S. T.; Hu, Z. G.; Wang, J. Y.; Wu, Y. C.; Halasyamani, P. S. $BaF_2TeF_2(OH)_2$: A UV Nonlinear Optical Fluorotellurite Material Designed by Band-Gap Engineering. *J. Am. Chem. Soc.* **2020**, *142*, 4616-4620.
(16) Feng, J. H.; Hu, C. L.; Xia, H. P.; Kong, F.; Mao, J. G. $Li_7(TeO_3)_3F$: A Lithium Fluoride Tellurite with Large Second Harmonic Generation Responses and a Short Ultraviolet Cutoff Edge. *Inorg. Chem.* **2017**, *56*, 14697-14705.
(17) Sykora, R. E.; Ok, K. M.; Halasyamani, P. S.; Albrecht-Schmitt, T. E. Structural Modulation of Molybdenyl Iodate Architectures by Alkali Metal Cations in $AMoO_3(IO_3)$ (A = K, Rb, Cs): a Facile Route to New Polar Materials with Large SHG Responses. *J. Am. Chem. Soc.* **2002**, *124*, 1951-1957.
(18) Wu, C.; Lin, L.; Jiang, X. X.; Lin, Z. S.; Huang, Z. P.; Humphrey, M. G.; Halasyamani, P. S.; Zhang, C. $K_5(W_3O_9F_4)(IO_3)$: An Efficient Mid-Infrared Nonlinear Optical Compound with High Laser Damage Threshold. *Chem. Mater.* **2019**, *31*, 10100-10108.
(19) Chang, H. Y.; Kim, S. H.; Halasyamani, P. S.; Ok, K. M. Alignment of Lone Pairs in a New Polar Material: Synthesis, Characterization, and Functional Properties of $Li_2Ti(IO_3)_6$. *J. Am. Chem. Soc.* **2009**, 131, 2426-2427.
(20) Sun, C. F.; Hu, C. L.; Xu, X.; Yang, B. P; Mao, J. G. Explorations of New Second-order Nonlinear Optical Materials in the Potassium Vanadyl Iodate System. *J. Am. Chem. Soc.* **2011**, *133*, 5561-5572.
(21) Chang, H. Y.; Kim, S. W.; Halasyamani, P. S. Polar Hexagonal Tungsten Oxide (HTO) Materials: (1) Synthesis, Characterization, Functional Properties, and Structure-Property Relationships in $A_2(MoO_3)_3(SeO_3)$ and (2) Classification, Structural Distortions, and Second-Harmonic Generating Properties of Known Polar HTOs. *Chem. Mater.* **2010**, *22*, 3241-3250.
(22) Zhang, J. J.; Tao, X. T.; Sun, Y. X.; Zhang, Z. H.; Zhang, C. Q.; Gao, Z. L.; Xia, H. B.; Xia, S. Q. Top-Seeded Solution Growth, Morphology, and Properties of a Polar Crystal $Cs_2TeMo_3O_{12}$. *Cryst. Growth Des.* **2011**, *11*, 1863-1868.
(23) Ra, H. S.; Ok, K. M.; Halasyamani, P. S. Combining Second-Order Jahn–Teller Distorted Cations to Create Highly Efficient SHG Materials: Synthesis, Characterization, and NLO Properties of $BaTeM_2O_9$. *J. Am. Chem. Soc.* **2003**, *125*, 7764-7765.
(24) Tang, R. L.; Hu, C. L.; Wu, B. L.; Fang, Z.; Chen, Y.; Mao, J. G. Cs_2 $Bi_2O(Ge_2O_7)$ (CBGO): A Larger SHG Effect Induced by Synergistic Polarizations of BiO_5 Polyhedra and GeO_4 Tetrahedra. *Angew. Chem. Int. Ed.* **2019,** *58*, 15358-15361.
(25) Ciupa-Litwa, A.; Zienkiewicz, J. A.; Stefanski, M.; Ptak, M.; Majchrowski, A.; Chruni, M. Vibrational and Optical Studies of a Nonlinear Optical Crystal, $Cs_2Bi_2O(Ge_2O_7)$, *Spectrochim. Acta, Part A*, **2021**, *259*, 119816.
(26) You, F. G.; Liang, F.; Huang, Q.; Hu, Z. G.; Wu, Y. C.; Lin, Z. S. $Pb_2GaF_2(SeO_3)_2Cl$: Band Engineering Strategy by Aliovalent Substitution for Enlarging Bandgap while Keeping Strong Second Harmonic Generation Response. *J. Am. Chem. Soc.* **2019**, *141*, 748-752.
(27) Wu, C. Wu, T. H.; Jiang, X. X.; Wang, Z. J.; Sha, H. Y.; Lin, L.; Lin, Z. S.; Huang, Z. P.; Long, X. F.; Humphrey, M. G.; Zhang, C. Large Second-Harmonic Response and Giant Birefringence of $CeF_2(SO_4)$ Induced by Highly Polarizable Polyhedra. *J. Am. Chem. Soc.* **2021**, *143*, 4138-4142.
(28) Lin, L.; Jiang, X. X.; Wu, C.; Li, L.; Lin, Z. S.; Huang, Z. P.; Humphrey, M. G.; Zhang, C. $Ba(MoO_2F)_2(XO_3)_2$ (X = Se and Te): First Cases of Noncentrosymmetric Fluorinated Molybdenum Oxide Selenite/Tellurite Through Unary Substitution for Enlarging Band Gaps and Second Harmonic Generation. *ACS Appl. Mater. Interfaces* **2020,** *12*, 49812-49821.
(29) Wu, C.; Li, L. H.; Lin, L.; Huang, Z. P.; Humphrey, M. G.; Zhang, C. Enhancement of Second-Order Optical Nonlinearity in a Lutetium Selenite by Monodentate Anion Partial Substitution. *Chem. Mater.* **2020**, *32*, 3043-3053.
(30) Halasyamani, P. S. Asymmetric Cation Coordination in Oxide Materials: Influence of Lone-Pair Cations on the Intra-Octahedral Distortion in d^0 Transition Metals. *Chem. Mater.* **2004**, *16*, 3586-3592.
(31) Sivakumar, T.; Chang, H. Y.; Baek, J.; Halasyamani, P. S. Two New Noncentrosymmetric Polar Oxides: Synthesis, Characterization, Second-Harmonic Generating, and Pyroelectric Measurements on $TlSeVO_5$ and $TlTeVO_5$. *Chem. Mater.* **2007**, *19*, 4710-4715; and references therein.
(32) Jin, C. G.; Wan, M. J.; Huang, L. X.; Shao, J. X.; Wang, F. H. Experimental and Theoretical Studies of Optical and Nonlinear Opti-

cal Properties for $MnTeMoO_6$ Crystal. *J. Alloys Compd.* **2015**, *651*, 585-589.
(33) Zhang, J. J.; Zhang, Z. H.; Zhang, W. G.; Zheng, Q. X.; Sun, Y. X.; Zhang, C. Q.; Tao, X. T. Polymorphism of $BaTeMo_2O_9$: A New Polar Polymorph and the Phase Transformation. *Chem. Mater.* **2011**, *23*, 3752-3761; and references therein.
(34) Zhang, J. J.; Zhang, Z. H.; Sun, Y. X.; Zhang, C. Q.; Zhang, S. J.; Liu, Y.; Tao, X. T. $MgTeMoO_6$: A Neutral Layered Material Showing Strong Second-Harmonic Generation. *J. Mater. Chem.* **2012**, *22*, 9921-9927.
(35) Goodey, J.; Broussard, J.; Halasyamani, P. S. Synthesis, Structure, and Characterization of a New Second-Harmonic-Generating Tellurite: $Na_2TeW_2O_9$. *Chem. Mater.* **2002**, *14*, 3174-3180.
(36) Kong F.; Mao, J. G. Recent progress in selenite and tellurite based SHG materials. *Dalton Trans.* **2020**, *49*, 8433-8437; and references therein.
(37) Zhao, S. G.; Jiang, X. X.; He, R.; Zhang, S. Q.; Sun, Z. H.; Luo, J. H.; Lin, Z. S.; Hong, M. C. A Combination of Multiple Chromophores Enhances Second-Harmonic Generation in a Nonpolar Noncentrosymmetric Oxide: $CdTeMoO_6$. *J. Mater.Chem. C* **2013**, *1*, 2906-2912; and references therein.

Table of Contents